Characterization and modeling of the damage mechanisms in ductile steel metal-matrix composites: Application to virtual forming

Pouya Tajdary, Khaoula Dorhmi, Léo Morin, Katell Derrien, Zehoua Hadjem-Hamouche, Chedly Braham, Jean-Pierre Chevalier

▶ **To cite this version:**

Pouya Tajdary, Khaoula Dorhmi, Léo Morin, Katell Derrien, Zehoua Hadjem-Hamouche, et al.. Characterization and modeling of the damage mechanisms in ductile steel metal-matrix composites: Application to virtual forming. Mechanics of Materials, 2023, 184, pp.104741. 10.1016/j.mechmat.2023.104741 . hal-04184132

HAL Id: hal-04184132

https://cnam.hal.science/hal-04184132v1

Submitted on 12 Dec 2023

HAL is a multi-disciplinary open access archive for the deposit and dissemination of scientific research documents, whether they are published or not. The documents may come from teaching and research institutions in France or abroad, or from public or private research centers.

L'archive ouverte pluridisciplinaire **HAL**, est destinée au dépôt et à la diffusion de documents scientifiques de niveau recherche, publiés ou non, émanant des établissements d'enseignement et de recherche français ou étrangers, des laboratoires publics ou privés.

Copyright

Characterization and modeling of the damage mechanisms in ductile steel metal-matrix composites: Application to virtual forming

Pouya Tajdary [a], Khaoula Dorhmi [a], Léo Morin [a,b,*], Katell Derrien [a], Zehoua Hadjem-Hamouche [a], Chedly Braham [a], Jean-Pierre Chevalier [a]

[a] PIMM, Arts et Metiers Institute of Technology, CNRS, Cnam, HESAM University, 151 boulevard de l'Hopital, 75013 Paris, France
[b] Université de Bordeaux, ENSAM, CNRS, Bordeaux INP, I2M, UMR 5295, F-33400, Talence, France

Keywords:
Fe-TiB_2 composites
Stiffness loss
Homogenization
Nakazima test

The aim of this work is to investigate the damage mechanisms and stiffness loss in Fe-TiB_2 metal-matrix composites during plastic deformation. First, experimental results of interrupted tensile tests are performed to quantify the evolution of damage, using SEM observations, as well as the decrease of Young's modulus as a function of the tensile strain. The experimental results are then used to calibrate a two-step homogenization model for metal-matrix composites in which the nucleation and growth of voids modify incrementally the overall elastic properties. The model is finally applied to the numerical prediction of stiffness loss in a problem of metal forming based on Nakazima tests. Overall, the stiffness loss predicted before the onset of coalescence is moderate and its distribution is homogeneous, emphasizing that Fe-TiB_2 metal-matrix composites could be used in applications requiring metal forming.

1. Introduction

Metal matrix composites (MMC) are promising materials and their use in industrial applications keeps growing (Chawla, 2012; Nicholls et al., 2017; Zhou et al., 2020). For weight reduction applications, MMC are particularly interesting because a significant increase of the specific modulus (E/ρ) can be reached when the reinforcing particles are stiffer and lighter than the matrix. Hence, those materials are of important interest in automotive and aeronautic industries to improve energy efficiency and decrease CO_2 emissions.

In this context, Fe-TiB_2 metal-matrix composites have been developed recently (Hadjem-Hamouche et al., 2012, 2018; Gaspérini et al., 2017). These materials are very interesting due to the very high elastic modulus of light TiB_2 particles (Okamoto et al., 2010). Recent improvements in continuous casting of this composite, achieved by modifications of the composition and the solidification rate, have led to a significantly finer particle distribution (Dorhmi et al., 2021). Then after casting, Fe-TiB_2 products are processed either by (i) hot rolling or (ii) hot rolling followed by cold rolling. A volume fraction of particles of about 10% leads to an increase of the specific stiffness of about 13% for the hot rolled products (Dorhmi et al., 2021).

An important drawback of metal matrix composites in structural applications is the occurrence of damage during plastic deformation which is generally due to the presence of brittle particles (Mortensen and Llorca, 2010). Indeed, the presence of particles with high volume fractions promotes the nucleation of voids (due to particle cracking and/or decohesion of the particle-matrix interfaces) which can be followed by void growth and coalescence after plastic straining. Therefore, plastic deformation in metal matrix composites is expected to induce microstructural modifications that would induce a decrease of the overall stiffness due to the presence of voids. As a result, MMC may lose their improved properties in processes requiring plastic deformation such as metal forming and rolling. Hence, an important challenge for MMC is to predict the evolution of damage and its influence on the overall elastic properties during complex processing routes; this would ultimately permit the design of optimal processing paths minimizing the damage occurrence. In addition, it must be noted that metallic alloys in general can also exhibit a reduction of their Young's modulus after plastic deformation (Morestin and Boivin, 1996; Chen et al., 2016b). Even though the reduction of their Young's modulus is generally lower than that observed for metal matrix composites, it can reach in some cases 20% for mild steels (Yoshida et al., 2002), high-strength steels (Cleveland and Ghosh, 2002) and dual-phase steels (Chen et al., 2016a).

The modeling of metal-matrix composites has mainly focused on the derivation of the overall elastic properties (Segurado and LLorca, 2002) or plastic properties (Ponte Castaneda and Suquet, 1997; González and

* Corresponding author at: Université de Bordeaux, ENSAM, CNRS, Bordeaux INP, I2M, UMR 5295, F-33400, Talence, France.
E-mail address: leo.morin@u-bordeaux.fr (L. Morin).

https://doi.org/10.1016/j.mechmat.2023.104741

Table 1
Chemical composition of the Fe-TiB_2 composite.

Element	C	Al	Cr	Mn	Ni	Si	Ti	B	P	Fe
Weight %	0.04	0.07	0.06	0.09	0.04	0.17	5.4	1.69	0.01	Bal.

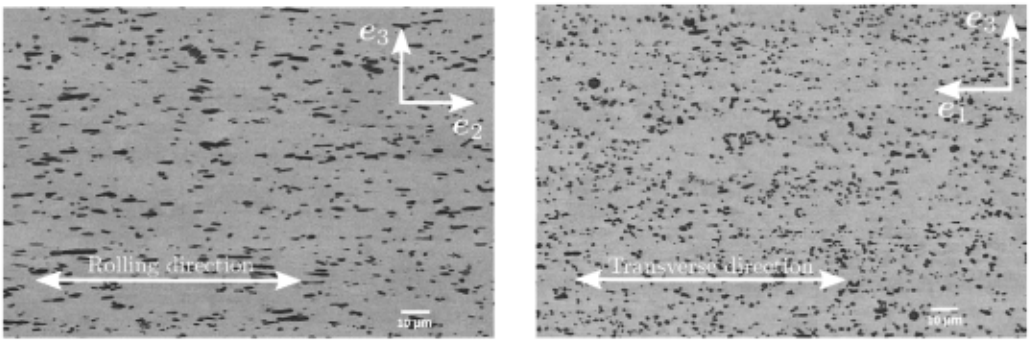

Fig. 1. SEM (image mode: BSE) micrographs of hot rolled Fe-TiB_2 composite (TiB_2 particles appear with dark contrast). (a) Plane (e_2, e_3) and (b) Plane (e_1, e_3).

LLorca, 2000; Doghri and Ouaar, 2003; Mueller and Mortensen, 2006), without damage. The derivation of models for MMC that include the effect of damage upon the elastic and/or plastic properties is scarce, and has mainly followed a phenomenological approach (Voyiadjis and Kattan, 1993). Several micromechanical models have been derived and permit in general to reproduce accurately macroscopic stress–strain curves but they do not permit to predict the loss of stiffness observed after plastic straining (LLorca et al., 1991; González and LLorca, 2000; Tekoglu and Pardoen, 2010). Mention has to be made to the work of Derrien et al. (1999) in which the decrease of the Young's modulus of Al-SiC composites is accounted for as a function of the tensile strain. However, the numerical prediction of the progressive stiffness loss in MMC during arbitrary loading paths (such as in forming processes) is a difficult task since it requires the development of a coupled elastic–plastic model including damage evolution. It should also be noted that, in the general context of ductile porous solids, the effect of ductile damage on the elastic stiffness is generally disregarded in micromechanical models such as in the GTN model, despite its importance in the simulation of forming processes (Saanouni, 2008), notably for reproducing springback (Wagoner et al., 2013); in the work of Yeh and Cheng (2003) related to metallic materials, Gurson's model is used to define a damage variable allowing the decrease of the elastic properties, but the model has only been applied to the simulation of tensile tests (and does not apply to metal-matrix composites).

Very recently, Dorhmi et al. (2020) derived a homogenization-based model that describes the progressive loss of stiffness in metal-matrix composites. In this model, the effect of damage on the elastic properties is described by a mean-field homogenization scheme, which depends on the volume fraction of the phases. Then the evolution of damage is driven by a Gurson-type model, which allows the description of the nucleation and growth of voids; the plasticity model is thus used to update the volume fractions of the phases which in turns modify the elastic properties. This model has permitted to reproduce accurately the stiffness loss observed experimentally in tensile tests of several metal composite materials (such as Al-SiC metal matrix composites and cast irons) and appears to be a good candidate for the simulation of complex strain paths and the prediction of the Young's modulus reduction induced by forming processes.

The aim of this work is to investigate the damage mechanisms in Fe-TiB_2 metal-matrix composites and simulate the effect of damage on the progressive stiffness loss during forming, using Dorhmi et al. (2020)'s homogenized model, based on Gurson's model. Experimental results based on tensile tests combined with SEM observations are used to assess the micromechanical model of Dorhmi et al. (2020). The model calibrated is then used in a model problem of metal forming in order to investigate numerically the heterogeneous degradation of the elasticity property during the process. The process is followed by a three-point bending test which allows the determination of a macroscopic property after processing. The objective is to assess the ability of an enriched Gurson-type model to simulate complex processes involving damage followed by a mechanical test, in a virtual design approach. Therefore, the approach considered is interesting from a fundamental point of view because virtual forming with damage is usually done using CDM-like models (which include the effect of damage on the elasticity properties) (Saanouni, 2008). The present work tackles for the first time the coupling between damage and elasticity properties in forming processing using a micromechanical Gurson-type model and constitutes an alternative to CDM models (which are phenomenological models by essence). The rest of the paper is organized as follows. In Section 2, experimental results of interrupted tensile tests are presented to characterize the evolution of damage in Fe-TiB_2 composites. Section 3 recapitulates the model of Dorhmi et al. (2020) and provides a calibration of its parameters. Finally, the virtual design of Fe-TiB_2 is investigated in Section 4 through numerical simulations of a forming process followed by a mechanical test in order to investigate damage and stiffness loss in Fe-TiB_2 composites during forming.

2. Experimental results

2.1. Material

We consider Fe-TiB_2 composites developed by ArcelorMittal (ARCELOR-Research-group, 2008) which have been designed for their high specific stiffness (E/ρ). After continuous casting, slabs of Fe-TiB_2 are hot rolled, and subjected to recrystallization annealing at 800° for 25 min (4 min of temperature rise and 21 min of holding time). The chemical composition is given in Table 1.

Back scattered electron imaging (BSE) with a SEM shows (Fig. 1) a ferritic matrix (light contrast) reinforced with particles elongated in the rolling direction (dark contrast). Two types of TiB_2 particles are present in the ferritic matrix: primary hexagonal particles, formed before eutectic transformation, and eutectic ones. In a previous work, Dorhmi et al. (2021) performed a microstructure analysis using images taken in two perpendicular planes, namely the plane (e_2, e_3) and the plane (e_1, e_3) where e_2 is the rolling direction (see Fig. 1). This has led to the classification of the particles according to their shape. Overall, the conclusions are that the particles are spheroidal with a major axis parallel to the rolling direction and the aspect ratio follows a

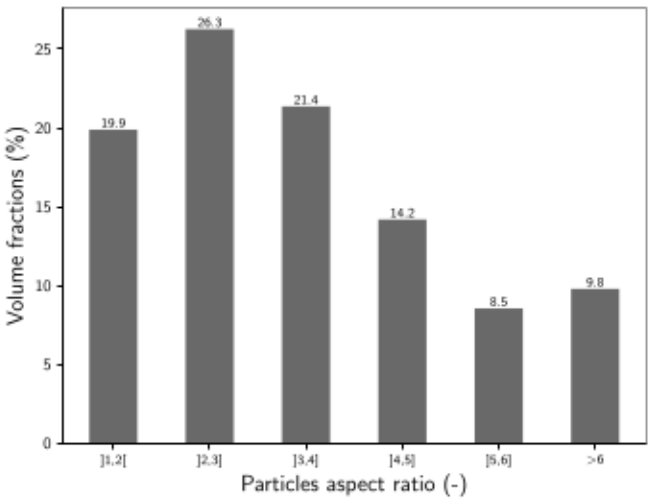

Fig. 2. Distribution of the particles' aspect ratios determined after microstructure analyses (Dorhmi et al., 2021).

distribution that is quite homogeneous in terms of volume fraction (see Fig. 2): (a) 20% of the total volume fraction of particles for those having an aspect ratio of 1, (b) 27% for particles having an aspect ratio of 2, (c) 23% of particles having an aspect ratio of 3, and finally (d) an average of 30% of particles having an aspect ratio of 6. The average aspect ratio is of about 3 which can be considered as moderate. In addition, the average volume fraction of particles is about $v_f = 10\%$ (Dorhmi et al., 2021).

It has been shown in Dorhmi et al. (2021) that the crystallographic texture in the matrix is small; the particles, on the other hand, are transverse isotropic in the rolling direction. The macroscopic elastic properties are isotropic (Dorhmi et al., 2021), with an initial value for the Young's modulus of about $E = 230$ GPa. This overall isotropic behavior is related to a competition between the anisotropic behavior of the particles and the spheroidal shape of the particles (see e.g. Derrien et al. (2018)).

2.2. Damage mechanisms during tensile tests

First, the fracture surfaces observed after a tensile test are characterized by an homogeneous distribution of dimples and the presence of fractured particles (Fig. 3). The dimples are related to the growth and coalescence of micro-voids which is typical in ductile materials. Most of the particles observed on the fracture surface appear to have fractured. The analysis of the fracture surfaces shows traces of fractured particles at the bottom of the dimples along the plane normal to the axis of solicitation.

Then, interrupted tensile tests were performed in the rolling direction (which coincides with the axis $\boldsymbol{e}_2$) in order to investigate the evolution of damage. The tests have been interrupted at several values of the tensile stress in order to (i) quantify the evolution of damage in surface using SEM observations and (ii) measure the evolution of Young's modulus as a function of the strain.

SEM observations have been performed in the same area of the specimen after unloading, as shown in Fig. 4. The void nucleation mechanism in Fe-TiB_2 composite is mainly due to particle cracking with in general a few cracks within a particle and no decohesion was observed. Cracks are nucleated at the very beginning of the plastic regime and open during plastic straining. Cracking occurs perpendicularly to the loading axis. It is worth noting that some nucleation of voids within the ferritic matrix, due to second-phase particles, are also observed.

The SEM observations have permitted to determine the percentage of particles that fracture in surface, denoted by c_{frac}, as a function of the tensile strain, and represented in Fig. 5a. This percentage corresponds to the number of fractured particles (with one or multiple cracks) normalized by the total number of particles. It has been determined using at least 10 SEM images per level of tensile strain in order to be statistically representative. At the beginning of the plastic deformation, a total of 3.5% of particles are fractured and this fraction of fractured particles reaches a maximal value of about 36% after a plastic deformation of 0.143. It is worth noting that half of the fractured particles appear at a strain of about $0.03 - 0.04$. In addition, acoustic emission in combination with quasi-static tensile testing was performed to complete the surface SEM observations (see Fig. 5b). The advantage of acoustic emission measurements is that it provides the damage evolution in the bulk; however the results of acoustic emission measurements are only qualitative because it accounts for all damage events: if multiple cracking occurs, the number of events recorded corresponds to the number of cracks and not the number of damaged particles. Overall, a good agreement is observed between the SEM image analyses of fractured particles and acoustic emission measurements.

Then, the evolution of Young's modulus, measured from the stress–strain curve (represented in Fig. 6a) during unloading, is represented in Fig. 6b. A double-sided extensometer (class 0.2) from Zwick (Clipon) was used. In order to determine the initial Young's modulus (before any plastic deformation), a sequence of two cycles of loading–unloading (at a load of about 80% of the yield stress) is done. The permits to eliminate (i) bending artifacts and (ii) anelasticity effects (such as microplasticity). Young's modulus is obtained during the (third) loading. Then, for the determination of Young's modulus during the tensile test, this previous procedure is not required anymore because bending artifacts and anelasticity effects are eliminated. Therefore, we only performed an unloading followed by a loading (at the stress before unloading). Young's modulus is thus determined during loading. Least squares fit is used on the linear elastic domain of loading to determine the Young's modulus (Dorhmi et al., 2021). The value for Young's modulus before deformation is of about 230 GPa and a loss of stiffness of 42 GPa is observed after 7% of deformation.

2.3. Summary of the experimental results

In order to calibrate the micromechanical model of Dorhmi et al. (2020), the main experimental results that will be used are summarized as follows:

- *Initial volume fractions.* The microstructural analysis performed by Dorhmi et al. (2021) leads to the value of the average volume fraction of particles $v_f = 10\%$. This value will be related to the volume fraction of nucleating voids.
- *Hardening behavior.* The stress–strain curve (Fig. 6a) will be used to calibrate the strain hardening curve. The softening part of the stress–strain curve (when necking takes place) will be used to calibrate the coalescence parameters.
- *Damage mechanisms.* The evolution of the fraction of fractured particles (Fig. 5a) will be used to calibrate the model of nucleation.
- *Young's modulus evolution.* The evolution of Young's modulus (Fig. 6b) will be used to adjust the calibration of the nucleation model and to calibrate the nucleation ratio of Dorhmi et al. (2021).

3. A homogenization-based damage model for metal-matrix composites

3.1. Description of the model

The model of Dorhmi et al. (2020) is based on an approximate two-step homogenization in which the elastic and plastic behaviors are treated separately. The elastic behavior does not induce damage

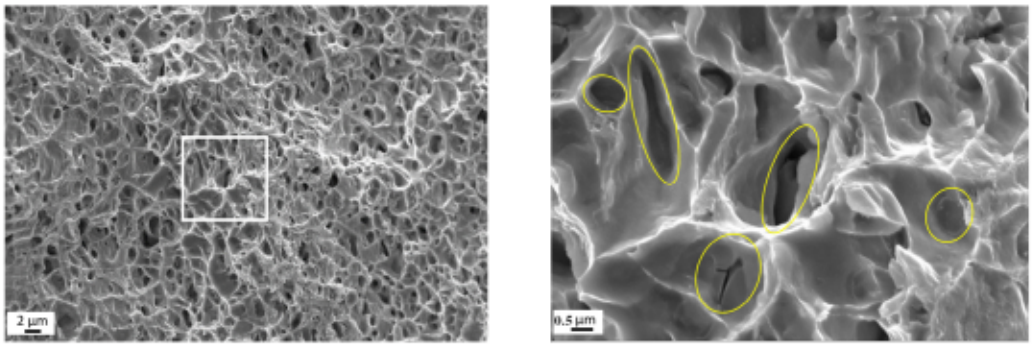

Fig. 3. Fracture surface of the Fe-TiB_2 composite. (a) Global view and (b) Enlarged view. The circles indicate fractured TiB_2 particles.

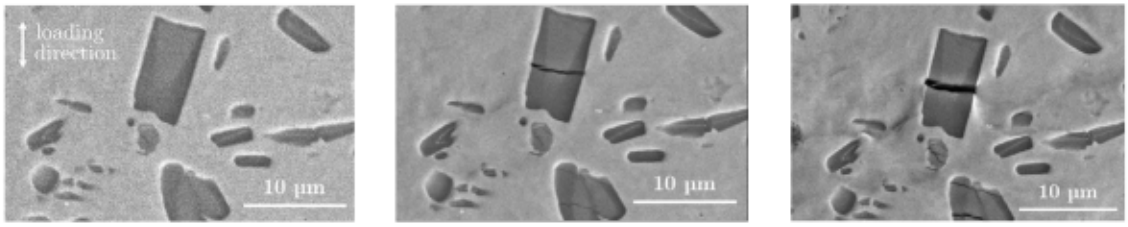

Fig. 4. SEM observations of the sequence of damage in interrupted tensile tests.

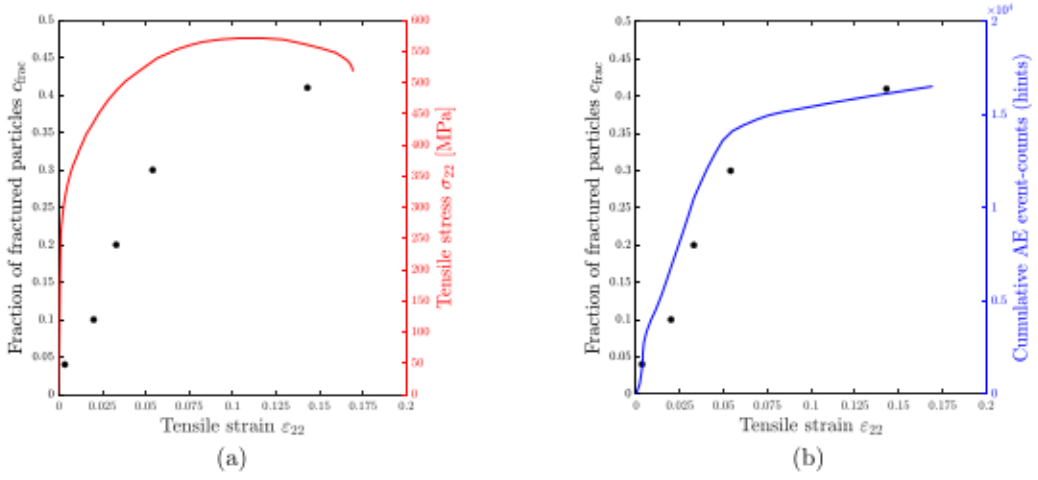

Fig. 5. Evolution of damage during tensile test. (a) Fraction of fractured particles determined by SEM observations in surface (represented by black circles). The stress–strain curve is shown in red. (b) Comparison between acoustic emission (AE) measurements (in blue) and the fraction of fractured particles (represented by black circles). (For interpretation of the references to color in this figure legend, the reader is referred to the web version of this article.)

which implies that the overall elastic properties depend only on the microstructure (volume fraction of the phases) *at a given instant*. The plastic behavior, on the other hand, induces damage in the form of nucleation and growth of microvoids during plastic straining. Therefore, the consequence of the damage evolution is a modification of the volume fractions of the phases which in turns modify incrementally the elastic properties (and allows the prediction of stiffness loss). The internal parameters of this model are thus the volume fractions of the phases (i.e. matrix, particles and cavities).

Homogenization of the elastic properties. The overall stiffness tensor $\mathbb{C}$ of the metal-matrix composite is given by the mean-field scheme of Mori and Tanaka (1973). We consider the case of a 3-phase composite made of an isotropic matrix (characterized by its shear and bulk moduli μ_m and κ_m), reinforced by isotropic spherical particles (characterized by its shear and bulk moduli μ_p and κ_p), and containing spherical voids. The internal parameters of the model are the volume fractions of the matrix, particles and voids, respectively denoted by f^m, f^p and f^v, where $f^m + f^p + f^v = 1$. The overall isotropic stiffness tensor is given by

$$\mathbb{C} = 3\kappa\mathbb{J} + 2\mu\mathbb{K} \tag{1}$$

where $\mathbb{J}$ is the spherical projection tensor and $\mathbb{K}$ the deviatoric projection tensor. The bulk modulus κ and shear modulus μ are given by Mori and Tanaka (1973)

$$\begin{cases} \kappa = \kappa_m \times \dfrac{f^m(\kappa_m + \alpha_m(\kappa_p - \kappa_m)) + f^p\kappa_p}{f^m(\kappa_m + \alpha_m(\kappa_p - \kappa_m)) + f^p\kappa_m + \dfrac{f^v}{1-\alpha_m}(\kappa_m + \alpha_m(\kappa_p - \kappa_m))} \\ \mu = \mu_m \times \dfrac{f^m(\mu_m + \beta_m(\mu_p - \mu_m)) + f^p\mu_p}{f^m(\mu_m + \beta_m(\mu_p - \mu_m)) + f^p\mu_m + \dfrac{f^v}{1-\beta_m}(\mu_m + \beta_m(\mu_p - \mu_m))} \end{cases}, \tag{2}$$

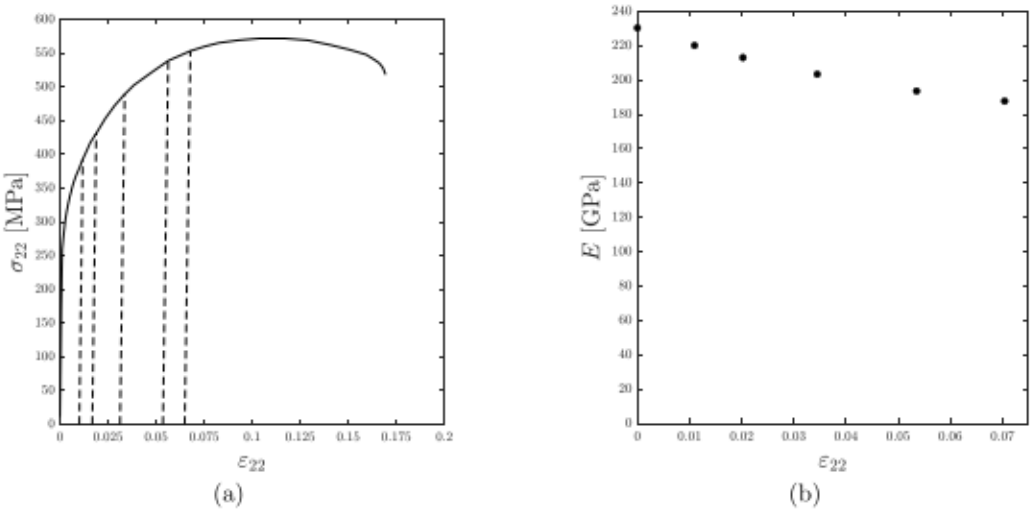

Fig. 6. Experimental results of interrupted tensile tests: (a) Stress–strain curves and (b) Stiffness loss evolution.

where α_m and β_m reads

$$\begin{cases} \alpha_m &= \dfrac{3\kappa_m}{3\kappa_m + 4\mu_m} \\ \beta_m &= \dfrac{6}{5}\dfrac{\kappa_m + 2\mu_m}{3\kappa_m + 4\mu_m}. \end{cases} \tag{3}$$

The Young's modulus and Poisson ratio of the metal-matrix composite are then simply given by

$$\begin{cases} E &= \dfrac{9\kappa\mu}{3\kappa + \mu} \\ \nu &= \dfrac{3\kappa - 2\mu}{2(3\kappa + \mu)}. \end{cases} \tag{4}$$

Homogenization of the plastic properties. First, it is assumed that the matrix obeys an isotropic von Mises yield criterion (with a yield stress denoted by σ_0^m) and that the particles remain elastic during plastic deformation. Therefore, it can be reasonably assumed that the system {matrix+particles} also follows a von Mises yield criterion (with a yield stress denoted by σ_0). This plasticity behavior of the sound metal-matrix composite is simply called "homogenized matrix". Then, the plastic behavior with voids is given by Gurson (1977)'s model. The macroscopic yield criterion reads

$$\Phi(\boldsymbol{\Sigma}) = \frac{\Sigma_{eq}^2}{\sigma_0^2} + 2qf^v \cosh\left(\frac{3\Sigma_m}{2\sigma_0}\right) - 1 - (qf^v)^2 \leq 0, \tag{5}$$

where Σ_{eq} is the macroscopic equivalent von Mises stress, Σ_m is the macroscopic mean stress (and thus σ_0 is the yield stress of the homogenized matrix). The parameter q is (classical) Tvergaard's parameters (Tvergaard, 1981; Tvergaard and Needleman, 1984). The macroscopic yield criterion is completed by a macroscopic flow rule obtained from the property of normality (which is preserved during scale transition):

$$\mathbf{D}^p = \dot{\lambda}\frac{\partial \Phi}{\partial \boldsymbol{\Sigma}}(\boldsymbol{\Sigma}) \quad , \quad \dot{\lambda}\begin{cases} = 0 & \text{if } \Phi(\boldsymbol{\Sigma}) < 0 \\ \geq 0 & \text{if } \Phi(\boldsymbol{\Sigma}) = 0 \end{cases} \tag{6}$$

where $\mathbf{D}^p$ denotes the plastic Eulerian strain rate and $\dot{\lambda}$ the plastic multiplier. Hardening is accounted for using Gurson (1977)'s heuristic approach; the constant yield stress σ_0 in the criterion (5) is replaced by some average yield stress $\overline{\sigma}$ given by

$$\overline{\sigma} = \sigma(\overline{\epsilon}), \tag{7}$$

where $\sigma(\epsilon)$ is the hardening function providing the yield limit as a function of the accumulated plastic strain ϵ, and $\overline{\epsilon}$ represents some average equivalent strain in the homogenized matrix. The evolution of $\overline{\epsilon}$ is given by the following equation

$$(1 - f^v)\overline{\sigma}\,\dot{\overline{\epsilon}} = \boldsymbol{\Sigma} : \mathbf{D}^p, \tag{8}$$

which corresponds to the (heuristic) assumption proposed by Gurson (1977) that the plastic dissipation in the porous material, $\boldsymbol{\Sigma} : \mathbf{D}^p$, is equal to that of a fictitious homogeneous material. Finally, the evolution equation of the porosity corresponding to the void growth mechanism is deduced from the matrix incompressibility:

$$\dot{f}_{\text{growth}} = (1 - f^v)\,\text{tr}\,\mathbf{D}^p. \tag{9}$$

Void nucleation. Void nucleation is described by the strain-controlled term of Chu and Needleman (1980)'s heuristic model. In the case of metal-matrix composites, void nucleation can be due to several mechanisms which are (i) the decohesion of matrix/particles interfaces, (ii) particle cracking and (iii) the void nucleation on second-phase particles. Here, it is assumed that each mechanism contributes to a total nucleation rate that is given by

$$\dot{f}_{\text{nucleation}} = \frac{f_N}{s_N\sqrt{2\pi}} \exp\left[-\frac{1}{2}\left(\frac{\overline{\epsilon} - \epsilon_N}{s_N}\right)^2\right] \times \dot{\overline{\epsilon}}, \tag{10}$$

where f_N, ϵ_N and s_N respectively represent the volume fraction, average nucleation strain and standard deviation of the *overall nucleating voids*.

Void coalescence. Void coalescence is classically accounted for by using Tvergaard and Needleman (1984)'s classical modification of Gurson (1977)'s model, which consists in replacing the porosity f by some larger fictitious one f^*, once some 'critical value' f_c has been reached:

$$f^* = \begin{cases} f & \text{if } f \leq f_c \\ f_c + \delta(f - f_c) & \text{if } f > f_c, \end{cases} \tag{11}$$

where f_c and $\delta > 1$ are material parameters.

Evolution equations of the internal parameters. The void growth and nucleation rates $\dot{f}_{\text{growth}}$ and $\dot{f}_{\text{nucleation}}$ are then connected to the volume fraction rates of the phases, $\dot{f}^m$, $\dot{f}^p$ and $\dot{f}^v$ by the equations

$$\begin{cases} \dot{f}^v &= \dot{f}_{\text{growth}} + \dot{f}_{\text{nucleation}} \\ \dot{f}^p &= -\theta\,\dot{f}_{\text{nucleation}} \\ \dot{f}^m &= -\dot{f}_{\text{growth}} - (1 - \theta)\dot{f}_{\text{nucleation}}, \end{cases} \tag{12}$$

where the parameter θ combines several nucleation mechanisms and corresponds to the overall nucleation ratio that permits to distinguish nucleation within the matrix and the particles. For instance, in the

Table 2
Parameters considered for the elastic properties and the initial volume fractions of the phases.

Elastic properties				Volume fractions		
E_p [GPa]	ν_p	E_m [GPa]	ν_m	f_0^v	f_0^p	f_0^m
583	0.11	210	0.3	0	0.1	0.9

particular case of decohesion of matrix/particles interfaces, the overall nucleation ratio takes the value $\theta = 1$ while in the particular case of void nucleation on second-phase particles, the overall nucleation ratio takes the value $\theta = 0$ (Dorhmi et al., 2020).

The model has been implemented numerically in the commercial finite element code Abaqus through a user material procedure (Umat and Vumat). The details of the algorithm used are provided in Appendix A.

Remark. It should be noted that in this model it is assumed that voids and particles are spherical. In practice, TiB_2 particles are spheroidal with an overall aspect ratio of about 3. However, it has been shown by Dorhmi et al. (2021) that the overall elastic behavior of the composite (in its initial state) is close to isotropy and it can be modeled using spherical particles. Indeed, the competition between the particles' elongation and their intrinsic anisotropy (which is isotropic transverse) makes their overall behavior isotropic (see e.g. Derrien et al. (2018)) and as a consequence they can be modeled by equivalent spherical particles with an isotropic elasticity behavior. In addition, the stress triaxiality of loadings considered in this work (tensile test and forming processes) is generally moderate ($T \geq 1/3$): void shape effects are thus expected to be moderate so that Gurson's model for spherical voids is suitable (Tajdary et al., 2022). Consequently, the present approach does not permit to account for induced-anisotropy of the elastic properties.

3.2. Calibration of the model parameters

The microstructure analysis performed by Dorhmi et al. (2021) shows that the composite considered contains about 10% of particles and no initial voids; therefore initially we consider the values $f_0^v = 0$, $f_0^p = 0.1$ and $f_0^m = 0.9$ for the volume fractions of the phases. The elastic constants considered are as follows: $E_m = 210$ GPa and $\nu = 0.3$ are considered for the ferritic matrix and $E_p = 583$ GPa and $\nu_p = 0.11$ are considered for the TiB_2 particles (Hadjem-Hamouche et al., 2018).

Then, we assume that the plastic behavior follows a Voce isotropic hardening law:

$$\sigma(\epsilon) = \sigma_y + Q\,(1 - \exp(-\beta\epsilon)) \tag{13}$$

where Q and β are the Voce hardening parameters and σ_y is the initial yield stress of sound composite. The calibrated values for the parameters σ_y, Q and β are given in Table 3.

The most difficult part concerns the calibration of the damage parameters. First, we calibrate the average nucleation strain ϵ_N and standard deviation s_N of the nucleation model by using the experimental fraction of fractured particles (as a function of the tensile strain). Indeed, there is a correlation between the evolution of the nucleating voids and the evolution of the fractured particles during deformation. Therefore, we calibrated ϵ_N and s_N so that the quantities $f_{\text{nucleation}}/\max(f_{\text{nucleation}})$ (of the model) and $c_{\text{frac}}/\max(c_{\text{frac}})$ (of the experiments) are in good agreement (see Fig. 7a).

Then several simulations of the tensile test were performed in order to find the remaining parameters that reproduce best both the experimental tensile test and the experimental stiffness loss. The calibrated set of parameters is given in Table 3. It should be noted that the value considered for the volume fraction of nucleating voids, $f_N = 0.14$, seems important. However, the volume fraction of nucleating voids that are *really* nucleated is in fact lower because of the values of the average nucleation strain ϵ_N and standard deviation s_N. Indeed, as shown in Fig. 7b, the normal distribution of the nucleated porosity is spread so that it is not null for a zero plastic strain. Therefore, the total nucleated porosity is $\max(f_{\text{nucleation}}) \sim 0.0962$, which is in the range of the initial volume fraction of particles. It is also interesting to note that the calibrated value for the parameter overall nucleation ratio is $\theta = 0.4$, which is in agreement with the experimental results since particle cracking was mostly observed (Dorhmi et al., 2020). Finally, it should be noted that a (classical) value $q = 1.25$ was considered for the model. Since the parameters related to nucleation (ϵ_N, s_N and f_N) are closely related to the modeling of stiffness degradation, a sensitivity analysis of their influence is provided in Appendix B: the values calibrated are not unique,[1] but they are consistent with the experimental observations.

The summary of all parameters is provided in Tables 2 and 3.

Once the damage and nucleation parameters are determined, the volume fractions of the phases can evolve during a plastic loading path (using Eqs. (12)) and the overall elastic properties can be updated using Eq. (3). In the case of tensile test, the model predictions (using the calibrated parameters) are compared to the experimental results in Fig. 8. Overall, a very good agreement is observed in both the stress–strain curve and the stiffness loss. The experimental results for the stiffness loss are almost contained in the envelope defined by the extreme values $\theta = 0$ and $\theta = 1$ (which are shown for illustrative purposes) and the optimal value is $\theta = 0.4$. It should be noted that the stress–strain curves are shown only for $\theta = 0.4$ because the parameter θ only modifies the elastic behavior after some plastic deformation and does not affect the plastic behavior.

4. Application to the virtual design of Fe-TiB_2 in a Nakazima forming test

In this section, the model calibrated and implemented in Section 3 is applied to the *virtual design* of Fe-TiB_2 sheets in a model problem of forming. The objectives of this numerical study are two-fold:

- The local degradation of Young's modulus of the metal matrix composites will be studied as a consequence of the heterogeneous distribution of the stress triaxiality;
- The consequence of this local stiffness loss will be discussed in terms of a macroscopic measure of the stiffness. Three-point bending tests will be performed after forming to study the influence of a local stiffness loss on the structural bending property.

It must be noted that, in this section, no comparison with experimental will be made because our objective is to study the local degradation of Young's modulus whose experimental "mapping" is not a trivial task (Bonnet and Constantinescu, 2005). Therefore, the results obtained only constitute *predictions* of the model, which are useful to assess (at least qualitatively) the effect of damage on elasticity properties during complex loading paths.

4.1. Description of the Nakazima test simulations

The model developed and calibrated in Section 3 will now be applied to the *numerical prediction* of the stiffness loss and failure of a Fe-TiB_2 sheet in an example of metal forming based on the Nakazima test. Indeed, the Nakazima test is widely used to study the forming limits of sheets for stress states ranging from uniaxial to equi-biaxial tension (see e.g. Amaral et al. (2017), Zhang et al. (2017), Gorji and Mohr (2018)). Therefore it constitutes an interesting tool to investigate the evolution of damage in Fe-TiB_2 metal-matrix composites during complex loading paths in which the triaxiality is heterogeneous.

The schematic of the Nakazima set-up is represented in Fig. 9. The testing procedure is composed of a hemispheric punch of 101.6 mm diameter and a blank holder which permits to hold the metal sheet

[1] As shown by Springmann and Kuna (2005), there is generally no unique set of material parameters for the GTN model.

Table 3
Parameters considered for the plastic properties and the damage parameters.

Plastic properties			Nucleation				Coalescence	
σ_y [MPa]	Q [MPa]	β	ϵ_N	s_N	f_N	θ	f_c	δ
300	380	28	0.02	0.04	0.14	0.4	0.105	18

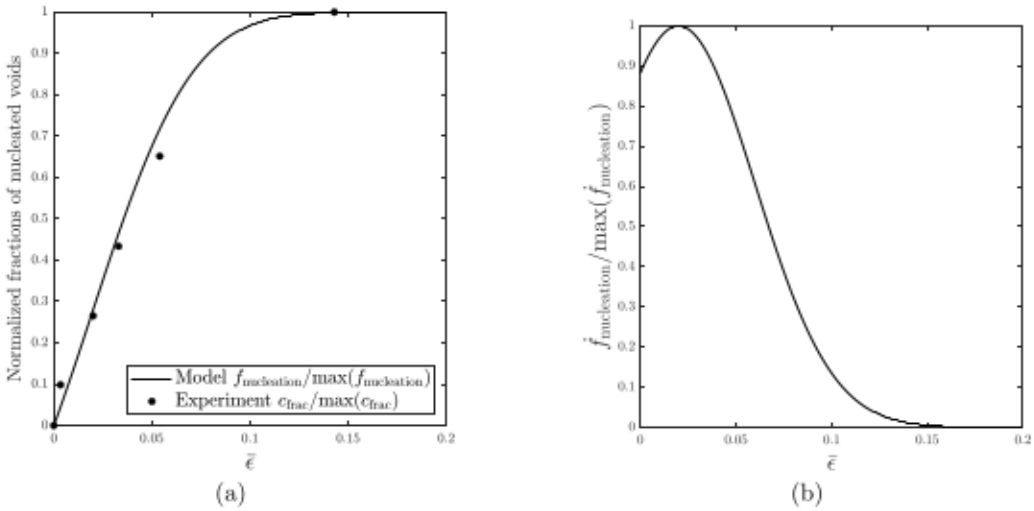

Fig. 7. Calibration of the nucleation parameters: (a) Normalized fraction of nucleating voids and (b) Normalized rate of nucleation.

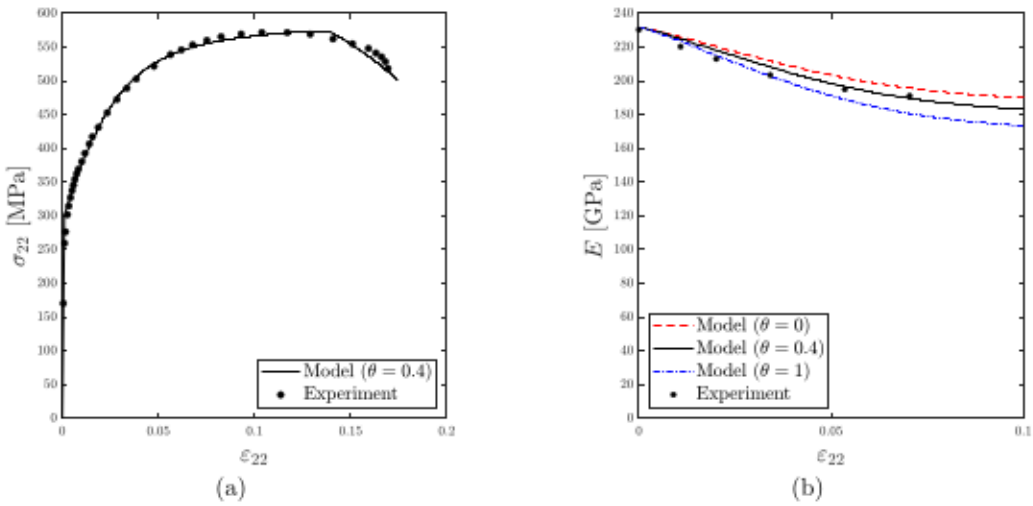

Fig. 8. Comparisons between experimental and model's predictions in a case of a tensile test: (a) stress–strain curves and (b) stiffness loss.

on the die. Several geometries for the sheets have been considered (cases W75, W125 and W170) and are represented in Fig. 10: this will permit to study different strain paths and stress states (with various triaxialities). The sheet metal blank has a thickness of 0.8 mm. The values considered for the geometry are typical of a Nakazima set-up for steels (Amaral et al., 2017).

A 3D finite element model of the Nakazima test has then been made using the commercial code ABAQUS/Explicit. Due to the symmetry of the process, only $1/4\,th$ of the specimen is considered. An example of mesh is provided in Fig. 11 for the case W75. The sheet metal is modeled as a 3D deformable part with selectively subintegrated 8-node trilinear brick (C3D8 elements in ABAQUS) which are suitable for quasi-incompressible plasticity. The punch, blank-holder and die are modeled as rigid 3D shells. Contact conditions are considered between the sheet and the rigid parts: the friction is accounted for by a Coulomb friction model in which the frictional force is related to the normal pressure applied on the surface. A value of 0.1 for the friction coefficient was used in the simulations, which is typical for lubricated steel–steel contact. It must be noted that friction has an notable role on failure during the Nakazima test (Zhang et al., 2017), so higher values could promote early damage.

The Nakazima test is performed numerically using a blank-holder force $F = 40$ kN in the case W75, $F = 82$ kN in the case W125 and $F = 164$ kN in the case W170. These blank-holder forces ensure a pressing of 0.1 μm for all cases. Several quantities will be studied in order to investigate the evolution of damage: (i) the distribution of the (heterogeneous) Young's modulus E in the whole specimen at several snapshots and (ii) the evolution of the porosity f^v, the volume fraction of particles f^p and Young's modulus E in the most damaged area (i.e. the Gauss point for which the porosity f^v is maximum at the end of the simulation).

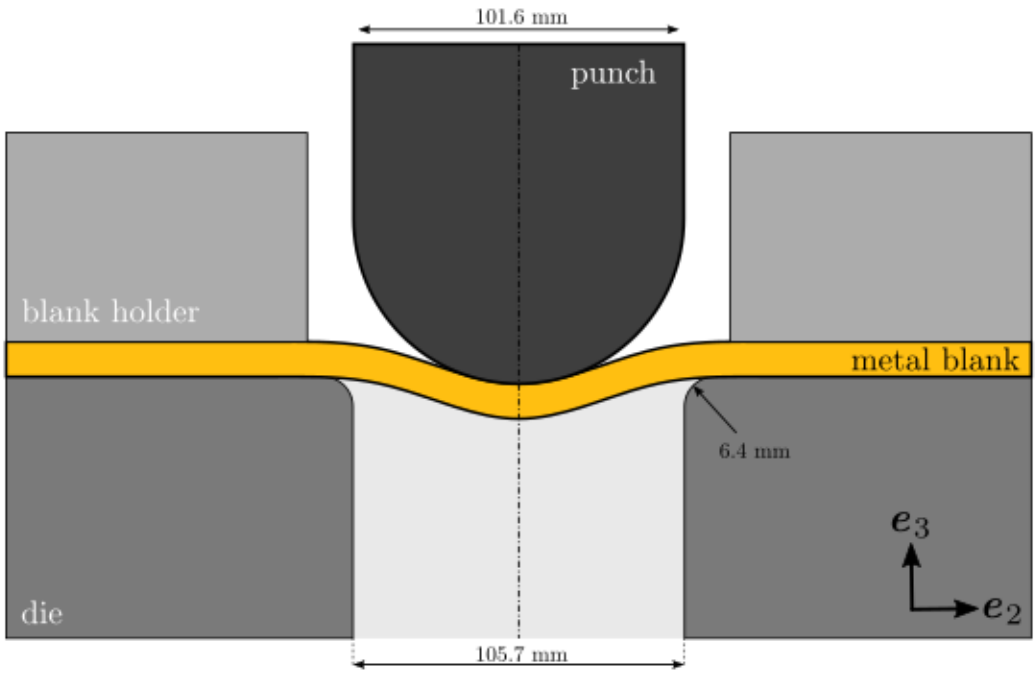

Fig. 9. Description of the Nakazima test simulations.

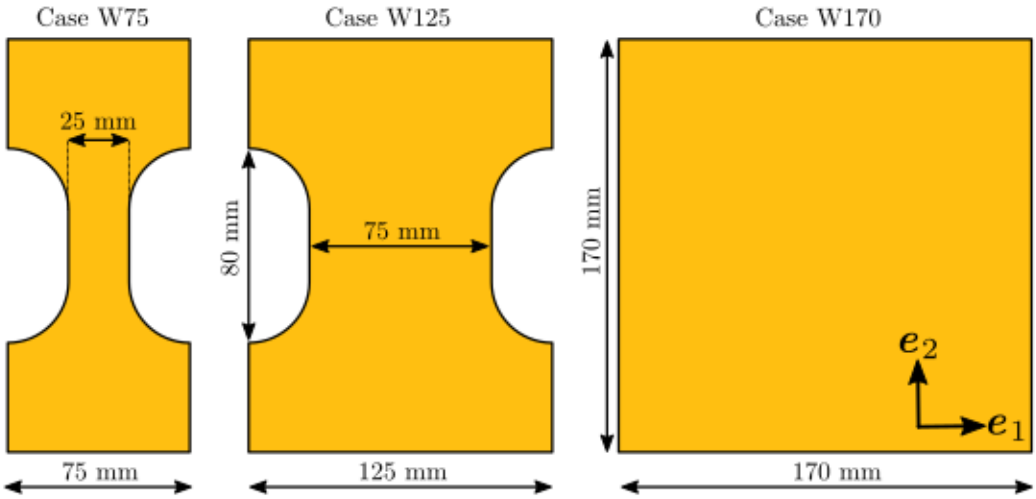

Fig. 10. Geometry of the specimens considered in the Nakazima test.

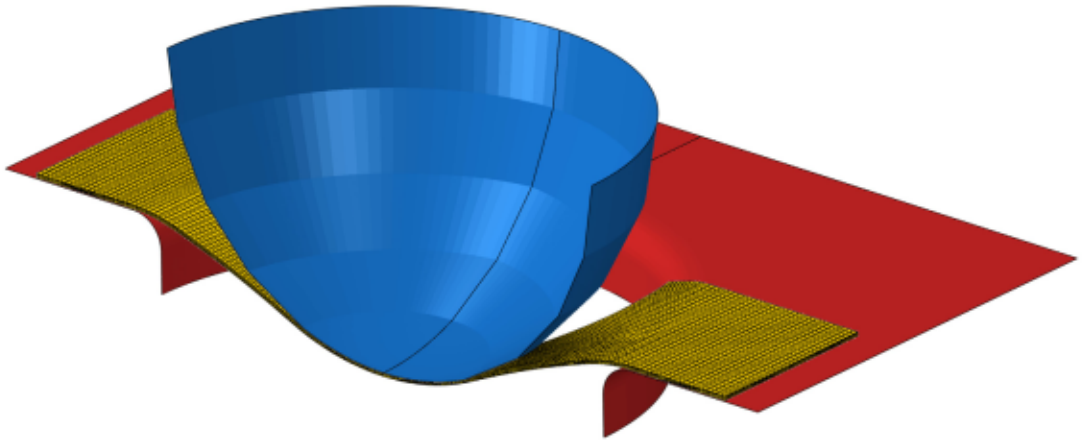

Fig. 11. Typical mesh considered for the Nakazima test in the case W75. The sheet metal, punch, blank-holder and die are composed of 16572 C3D8, 4178 R3D4, 2460 R3D4 and 2747 R3D4 elements, respectively.

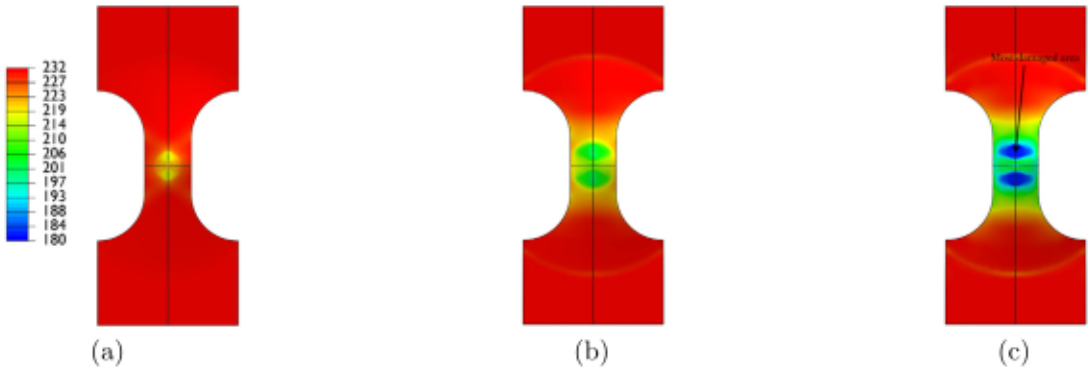

Fig. 12. Distribution of Young's modulus in the case W75. (a) Punch displacement $u_P = 5$ mm, (b) Punch displacement $u_P = 10$ mm and (c) Punch displacement $u_P = 14.91$ mm (just before failure).

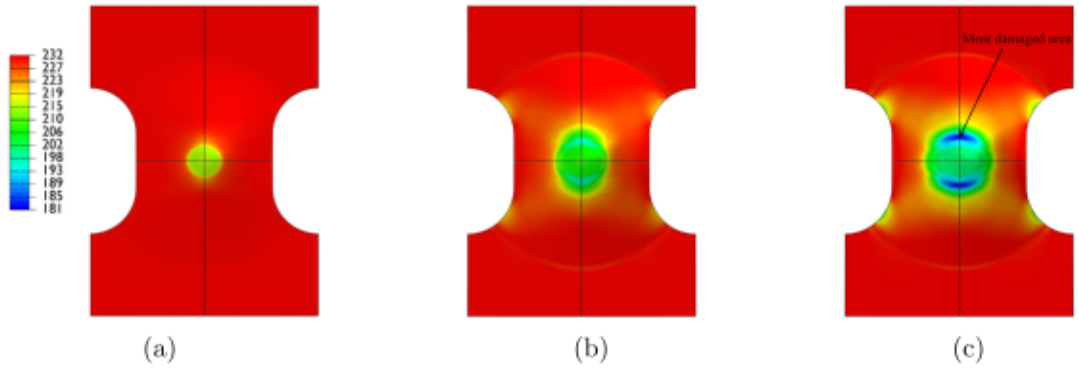

Fig. 13. Distribution of Young's modulus in the case W125. (a) Punch displacement $u_P = 5$ mm, (b) Punch displacement $u_P = 10$ mm and (c) Punch displacement $u_P = 12.53$ mm (just before failure).

4.2. Results of the Nakazima test

The simulations end for a punch displacement of about $u_P = 14.91$ mm, $u_P = 12.53$ mm and $u_P = 14.71$ mm, respectively for the cases W75, W125 and W170. The final stage of the fracture process becomes unstable with a brutal softening and very high values of the porosity. It is interesting to note that the punch displacements predicted numerically are roughly 1.5 times lower than the displacements typically observed in advanced dual phase steels (see e.g. Amaral et al. (2017) for a DP780 steel). Therefore, the ductility during forming predicted numerically for Fe-TiB_2 metal-matrix composites is quite reasonable, considering the presence of hard and brittle particles.

The distribution of the macroscopic (heterogeneous) Young's modulus E is represented for several punch displacements in Figs. 12–14, for the cases W75, W125 and W170, respectively. For moderate punch displacements, the decrease of Young's modulus is quite homogeneous in the area that is deformed plastically and is about 30 GPa (for $u_P = 10$ mm in all cases). Once there is void coalescence (i.e. when the porosity f becomes higher than the critical porosity f_c), the porosity reaches very high values in localized areas (corresponding to the macroscopic crack); as expected in those areas, the decrease of Young's modulus becomes very important due to the crack occurrence (see Figs. 12c, 13c and 14c).

In addition, the distribution of the stress triaxiality $T = \Sigma_m/\Sigma_{eq}$, is represented in Fig. 15 for each case (W75, W125 and W170) at a punch displacement $u_P = 10$ mm. As expected, the stress triaxiality is heterogeneous and overall it increases for large Nakazima specimens. The maximum values of the stress triaxiality are about $T \approx 0.66$, $T \approx 0.66$ and $T \approx 0.7$, respectively for W75, W125 and W170. In each case, the location of the maximum values of the stress triaxiality coincides with the area of maximum damage because void growth is mainly driven by the stress triaxiality.

Then, for illustrative purposes, the evolution of internal parameters of the model (the porosity f^V, the volume fraction of particles f^p and the Young's modulus E) are represented in Fig. 16, in the most damaged area of each specimen (which corresponds to the Gauss point having the maximum value of the porosity f^V at the end of the calculation, represented in Figs. 12c, 13c and 14c). This permits to quantitatively track the evolution of damage as a function of the punch displacement. Although the local stress state is different, the decrease of the particle volume fraction and the increase of the porosity are similar in all cases. It must be noted that the internal parameters do not vary at the beginning of the simulation because the Gauss point considered (which is different in each case since it is not located in the same area) remains elastic. Then the parameters evolve with a slope that is different from one case to another because the stress triaxiality is different in each case. Furthermore, for a given case, the slope is not constant because the triaxiality is not constant during the process. At the final failure (for a punch displacement between 12.5 mm and 14.9 mm according to the case considered), the volume fraction of particles is of about 0.06, which means that a significant proportion of particles are damaged during plastic deformation. Nonetheless, for moderate punch displacements (below 4 and 8 mm), the volume fraction of particles is generally higher than 0.08 and the overall Young's modulus higher than 210 GPa.

These numerical results show that during forming, Fe-TiB_2 metal-matrix composites exhibit a decrease of the Young's modulus which is localized in the area deformed by the punch. This decrease is heterogeneous and depends on the local loading state (through the stress triaxiality). For moderate forming levels (i.e. for punch displacements lower than 10 mm), the loss of stiffness is in general lower than

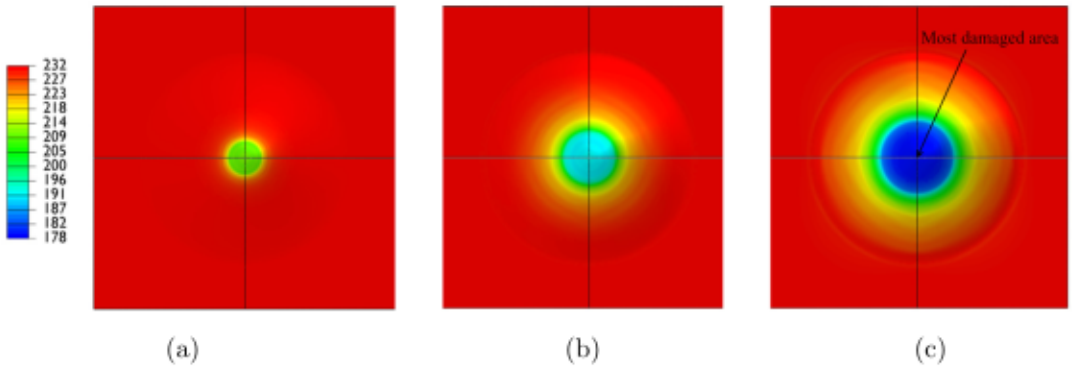

Fig. 14. Distribution of Young's modulus in the case W170. (a) Punch displacement $u_P = 5$ mm, (b) Punch displacement $u_P = 10$ mm and (c) Punch displacement $u_P = 14.71$ mm (just before failure).

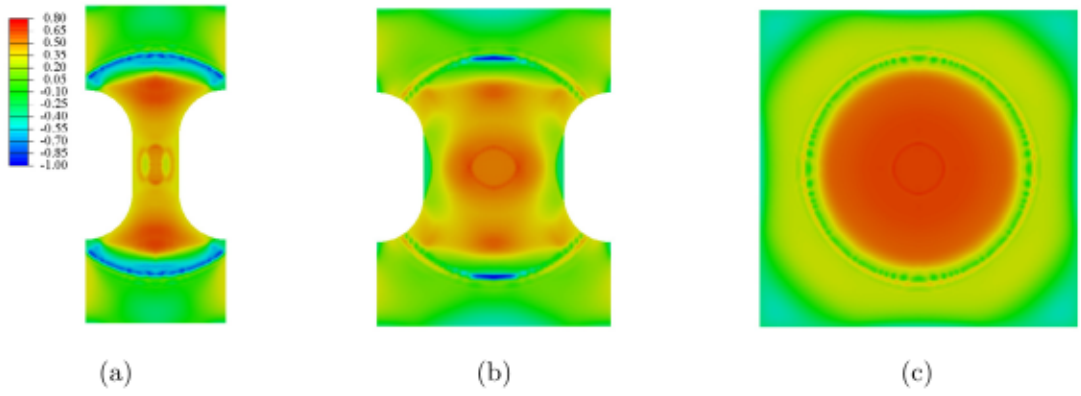

Fig. 15. Distribution of the stress triaxiality T at a punch displacement $u_P = 10$ mm. (a) Case W75, (b) Case W125 and (c) Case W170.

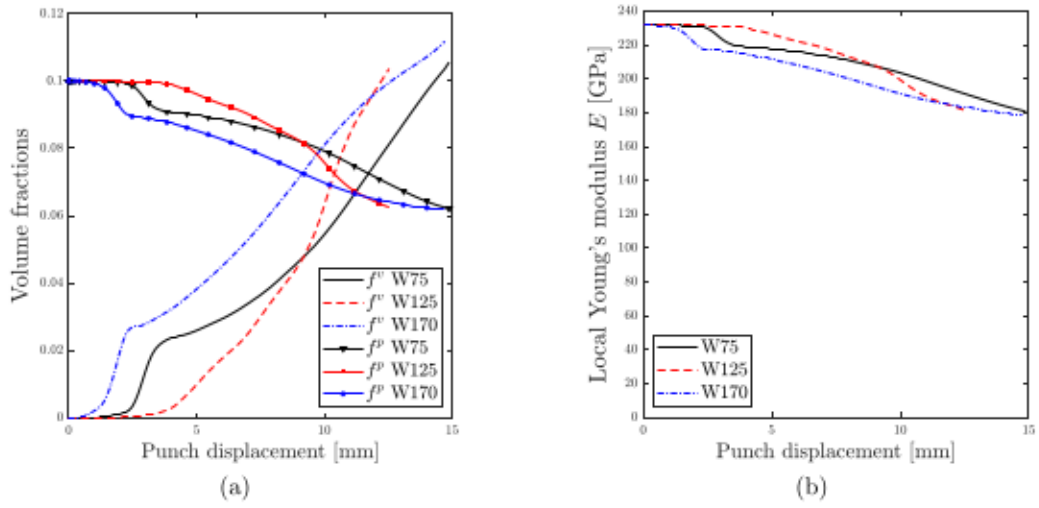

Fig. 16. Evolution of internal parameters in the integration point that fails first in the simulation of the Nakazima test. (a) Porosity f^v and volume fraction of particles f^p and (b) Young's modulus E.

30 GPa; therefore after forming, the Young's modulus can become lower than 210 GPa in some areas of the specimen. Hence, one can naturally question the relevance of Fe-TiB_2 metal-matrix composites over a steel (with $E = 210$ GPa) because the Young's modulus of Fe-TiB_2 can become locally lower to that of a steel, due to the occurrence of damage. Nonetheless, since in this application the stiffness loss in Fe-TiB_2 is localized in the area deformed by the punch, it may have little influence on a macroscopic measure of the stiffness, such as the structural bending stiffness.

4.3. Consequences on the overall bending structural stiffness

In practical structural applications, the stiffness property that is looked for is not the local distribution of Young's modulus in a specimen but a macroscopic measure of the stiffness such as for instance the *overall bending structural stiffness*. Therefore, it is of interest to study this overall bending stiffness of the specimens processed by the Nakazima test; this will allow the investigation of the consequence of a

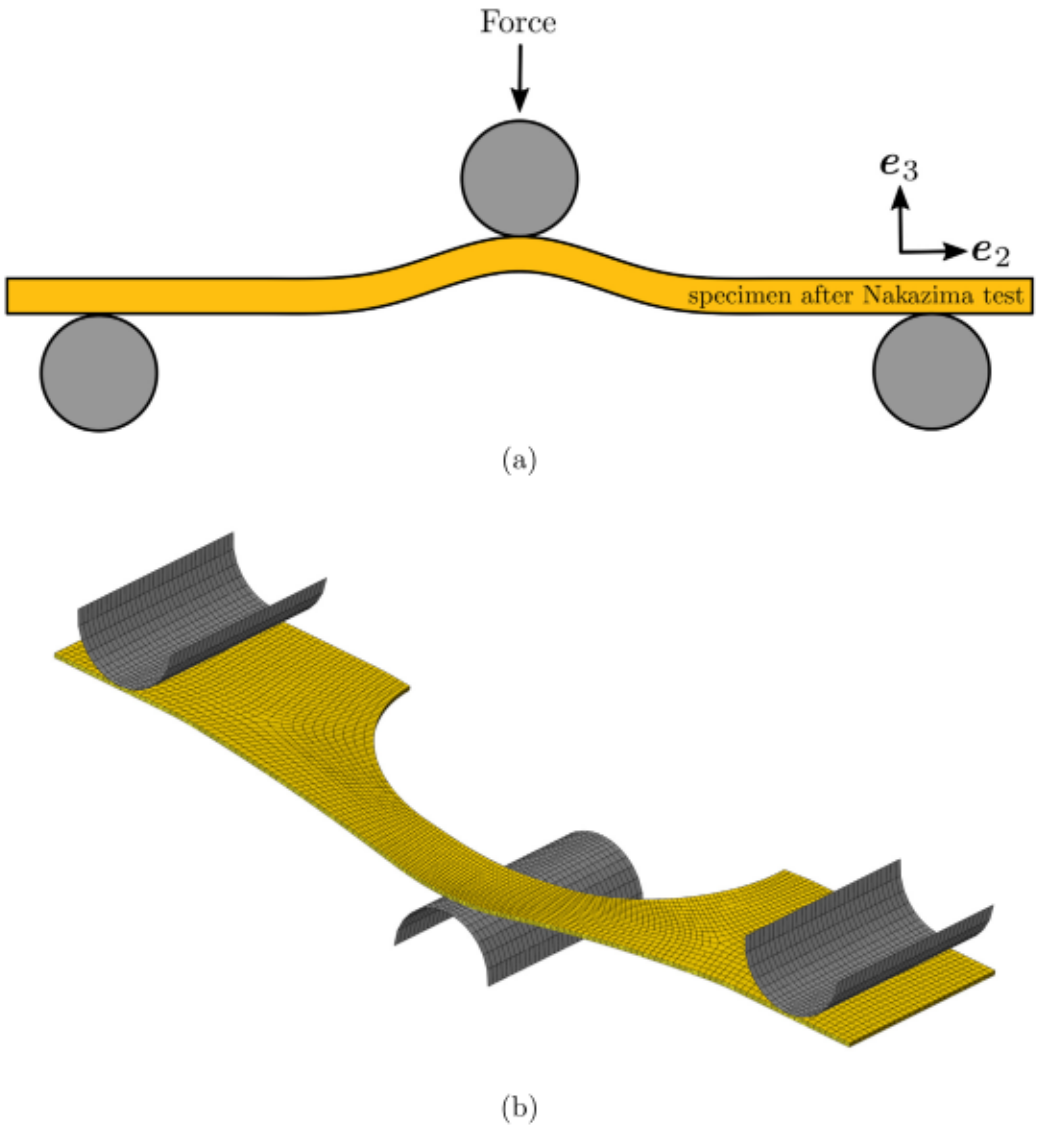

Fig. 17. Three-point bending test. (a) Description of the set-up and (b) Mesh considered in the case W75. The pins are composed of 660 R3D8 elements.

local degradation of Young's modulus on a macroscopic (engineering) property.

The overall bending stiffness will be determined by a numerical three-point bending test,[2] as sketched in Fig. 17a. It must be noted that other mechanical tests (such as tensile test in the direction e_2 for instance) could also have been performed, but since in practical applications Fe-TiB_2 composites are expected to be subjected to bending loads (Bonnet et al., 2014), it is of interest to consider a bending test. We consider rigid cylindrical pins in the direction x_1. The distance between the supporting pins is 143 mm. The bending stiffness K is then defined as

$$K = \frac{F}{u_z}, \tag{14}$$

where F is the force of the loading pin and u_z is the displacement of the specimen in the x_3-direction. In practice, the bending stiffness K is calculated numerically using the slope of the force–displacement curve $(F - u_z)$ in the linear elastic regime only determined by a numerical three-point bending test (see Fig. 17b for an example of mesh).

[2] Since analytical formula for the bending stiffness can only be derived for simple geometries, it will be determined numerically since the specimens considered have a complex shape after the Nakazima test.

The bending stiffness K will be determined for each type of Nakazima specimen (W75, W125 and W170) in three cases: (i) after no punch displacement ($u_P = 0$ mm), (ii) after a small punch displacement ($u_P = 5$ mm) and (iii) after a moderate punch displacement ($u_P = 10$ mm). Since the raw values of K cannot really be compared between each others (because in each case the geometry is different due to the type of specimen as well as the level of forming), we will compare the overall stiffness obtained for the Fe-TiB_2 to the stiffness of a *fictitious steel material* (without damage). This will permit to assess the effect of a heterogeneous decrease of Young's modulus after mechanical processing of Fe-TiB_2, in comparison to a steel with no damage. Therefore, we will study the ratio

$$\frac{K_{\text{Fe-TiB}_2}}{K_{\text{steel}}} \tag{15}$$

where $K_{\text{Fe-TiB}_2}$ is the bending stiffness corresponding to a specimen made of a Fe-TiB_2 material (sensitive to damage) after a Nakazima test and K_{steel} is the bending stiffness corresponding to a steel not sensitive to damage (i.e. with $E = 210$ GPa) subjected to the same Nakazima test. For simplicity we consider that the fictitious steel material has the same hardening properties than the Fe-TiB_2.

The ratio $K_{\text{Fe-TiB}_2}/K_{\text{steel}}$ is represented in Fig. 18 for each type of Nakazima specimen at the punch displacements $u_P = 0$ mm, $u_P = 5$ mm

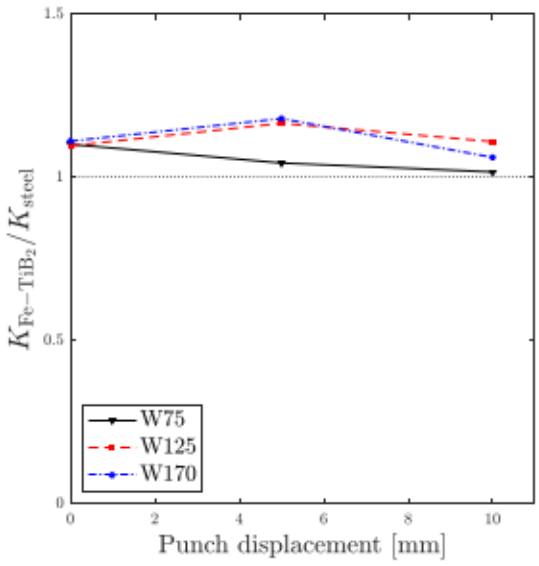

Fig. 18. Overall bending stiffness ratio $K_{\text{Fe-TiB}_2}/K_{\text{steel}}$ for several punch displacements.

and $u_P = 10$ mm. As expected the ratio (15) is greater than 1 before forming (at $u_P = 0$ mm) in all cases because without initial damage the Young's modulus of the Fe-TiB_2 is homogeneous and higher than that of the steel material. Interestingly, for the two levels of forming considered ($u_P = 5$ mm and $u_P = 10$ mm), the ratio $K_{\text{Fe-TiB}_2}/K_{\text{steel}}$ is also always higher than 1 for the three geometries considered. Thus in this application, Fe-TiB_2 materials provide higher overall elastic properties in comparison to a (non-damaged) steel, despite their locally degraded Young's modulus (which can be lower than 210 GPa). This macroscopic behavior observed can be explained by the fact that the overall bending elastic property does not depend only on the local properties but also on the elastic properties in the entire domain (as well as the geometry). Therefore, it can be concluded that for this application the local stiffness loss simulated numerically during forming of Fe-TiB_2 materials has only a little influence on the overall bending stiffness, provided that the stiffness loss is moderate. This result suggests that Fe-TiB_2 materials could constitute an interesting alternative to steels, even after forming. For higher forming levels, the ratio $K_{\text{Fe-TiB}_2}/K_{\text{steel}}$ will necessarily become lower than 1, due to the presence of damage. Nonetheless, it should be noted that, for typical structural parts, the deformation is more localized than in the Nakazima test. Therefore, in practical applications of Fe-TiB_2, the size of the area sensitive to damage is expected to be much smaller, and thus the associated macroscopic stiffness is expected to be little affected by damage.

5. Discussion

The Fe-TiB_2 metal-matrix composites considered in this work was found to have very interesting initial elasticity property ($E = 230$ GPa) and a good ductility. Indeed, the strain at the ultimate tensile stress is about 0.1 and the strain to fracture is about 0.18. The experimental results from tensile tests have been used to calibrate the micromechanical model of Dorhmi et al. (2020). The ductility determined numerically during Nakazima tests, using this model, is about 1.5 times lower than that observed in dual phase steels (Amaral et al., 2017), which can still be considered as important considering the presence of hard TiB_2 particles.

The numerical results of the Nakazima test using the model of Dorhmi et al. (2020) have shown that the local Young's modulus of Fe-TiB_2 metal-matrix composites is likely to decrease when the level of forming increases. It has been shown that the decrease of the Young's modulus is mostly localized in the area subjected to the punch displacement, so a large part of the specimen remains intact. Since in practical structural applications, only the *overall stiffness* is generally looked for, the consequence of this local decrease of Young's modulus on the bending stiffness has been studied and it has been shown that Fe-TiB_2 metal-matrix composites should keep improved properties in comparison with a 'non-damaged fictitious steel', for moderate forming levels. This observation is only valid in the case of the bending stiffness as other conclusions could be drawn depending on the characterization test (such as e.g. a tensile test) after forming.

However, it is important to note that for the comparison of the overall bending stiffness, the assumption of a *non-damaged* fictitious steel (i.e. with a Young's modulus equal to 210 GPa during forming) is not realistic. Indeed, this hypothesis is in general not verified for a large range of steels since a reduction of Young's modulus in steels[3] is generally observed after plastic deformation (Morestin and Boivin, 1996; Chen et al., 2016b). For instance, after 5% of deformation the reduction of Young's modulus can reach 20% for mild steels (Yoshida et al., 2002), high-strength steels (Cleveland and Ghosh, 2002) and dual-phase steels (Chen et al., 2016a). Therefore, since we assumed that the 'fictitious steel' is non-damaged, the comparison made in Section 4.3 has been performed in the worst possible conditions for the Fe-TiB_2 material; in practice, it is thus likely that Fe-TiB_2 materials will keep interesting properties even after high forming levels as steels will also exhibit a reduction of their modulus. It should be noted that such study cannot be performed in a systematic way since it would require to select a specific steel (having its specific reduction of Young's modulus) to make the comparison.

6. Conclusion

The aim of this work was to investigate the damage mechanisms in Fe-TiB_2 metal-matrix composites after plastic deformation. First, experimental results of interrupted tensile tests have been performed to quantify the fraction of fractured particles using SEM observations and the associated decrease of Young's modulus as a function of the tensile strain. The stiffness loss observed during the tensile test is about 16% for a tensile strain of 5%. Then the experimental results obtained have been used to calibrate the two-step homogenization model of Dorhmi et al. (2020). In this model, the volume fractions of the phases (matrix, particles and cavities) are internal parameters, used to determine the overall elastic properties through a Mori–Tanaka's scheme, and evolved by plastic deformation following the mechanisms of nucleation, growth and coalescence. The calibrated model has been applied to the numerical prediction of stiffness loss in the Nakazima test. Overall, the stiffness loss predicted before the onset of coalescence is moderate and it is localized in the area most deformed by the punch. Finally, the effect of this heterogeneous stiffness loss on the overall bending stiffness has been assessed: for moderate levels of forming, Fe-TiB_2 composites are expected to keep interesting elastic properties in comparison with non-damaged steels. The present results should be complemented by experimental observations on Fe-TiB_2 sheets subjected to Nakazima tests.

It should be noted that, for important levels of forming, the Young's modulus of Fe-TiB_2 composites can become lower than that of (non-damaged) steels. Nonetheless, since steels also exhibit a reduction of their Young's modulus after plastic deformation (Chen et al., 2016b), their elastic properties are also expected to decrease during forming, emphasizing that the use of steel-based metal matrix composites in forming applications is very promising.

[3] Similar reductions of Young's modulus after plastic deformation are also observed in aluminum alloys (Cleveland and Ghosh, 2002).

Declaration of competing interest

The authors declare that they have no known competing financial interests or personal relationships that could have appeared to influence the work reported in this paper.

Data availability

Data will be made available on request

Acknowledgments

This work is supported by the Carnot Institut Arts. Fruitful discussions with F. Bonnet are gratefully acknowledged.

Appendix A. Numerical implementation of Dorhmi's model

Following Dorhmi et al. (2020) (see also Enakoutsa et al. (2007)), the existence and uniqueness of the solution of the projection problem are ensured, provided that (i) the evolution equations of ϵ (the total strain) and $\overline{\epsilon}$ (the hardening parameter) are discretized in time with an implicit-scheme; (ii) the additional terms due to the objective time-derivative of $\boldsymbol{\Sigma}$ (in the hypoelasticity law) are discretized in time with an explicit-scheme; (iii) the values of f^v, f^p and f^m used in the criterion, the flow rule and the elastic behavior are those at the preceding time-step.

The discretized equations of the local projection problem are thus given by

$$\begin{cases} \boldsymbol{\Sigma}_{n+1} & = \boldsymbol{\Sigma}^{\text{elas}}_{n+1} - (3\kappa_n \mathbb{J} + 2\mu_n \mathbb{K}) : \Delta\boldsymbol{\epsilon}^{\text{p}}_n \\ \Phi(\boldsymbol{\Sigma}_{n+1}, f^v_n, \overline{\sigma}_{n+1}) & \leq 0 \\ \Delta\boldsymbol{\epsilon}^{\text{p}}_n & = \Delta\lambda_n \dfrac{\partial \Phi}{\partial \boldsymbol{\Sigma}}(\boldsymbol{\Sigma}_{n+1}, f^v_n, \overline{\sigma}_{n+1}) \\ \Delta\lambda_n & \geq 0 \\ \Delta\lambda_n \Phi(\boldsymbol{\Sigma}_{n+1}, f_n, \overline{\sigma}_{n+1}) & = 0 \\ \overline{\sigma}_{n+1} & = \sigma(\overline{\epsilon}_n + \Delta\overline{\epsilon}_n) \\ (1 - f^v_n)\overline{\sigma}_{n+1}\Delta\overline{\epsilon}_n & = \boldsymbol{\Sigma}_{n+1} : \Delta\boldsymbol{\epsilon}^{\text{p}}_n, \end{cases} \tag{A.1}$$

where $\kappa_n = \kappa(f^v_n, f^p_n, f^m_n)$ and $\mu_n = \mu(f^v_n, f^p_n, f^m_n)$ are the elastic moduli calculated for the previous microstructure and $\boldsymbol{\Sigma}^{\text{elas}}_{n+1} = \boldsymbol{\Sigma}_n + (3\kappa_n \mathbb{J} + 2\mu_n \mathbb{K}) : \Delta\boldsymbol{\epsilon}_n$ is the elastic predictor, that is the stress tensor at time t_{n+1} resulting from the strain increment $\Delta\boldsymbol{\epsilon}_n$ fictitiously considered as purely elastic.

The algorithm of solution thus consists in finding $\overline{\sigma}_{n+1}$ and $\Delta\lambda_n$ (see e.g. Morin et al. (2015)). First, the treatment of hardening is done using a fixed point method: (i) assume $\overline{\sigma}_{n+1} = \overline{\sigma}_n$; (ii) compute $\boldsymbol{\epsilon}^{\text{p}}_{n+1}$, $\boldsymbol{\Sigma}_{n+1}$ and $\overline{\epsilon}_{n+1}$ with this value $\overline{\sigma}_{n+1}$; (iii) deduce from Eq. $(A.1)_6$ a refined estimate of $\overline{\sigma}_{n+1}$; (iv) follow the procedure until the method converges and $\overline{\sigma}_{n+1}$ reaches a stationary value. The problem thus reduces to the determination of $\boldsymbol{\epsilon}^{\text{p}}_{n+1}$, $\boldsymbol{\Sigma}_{n+1}$ and $\overline{\epsilon}_{n+1}$, for a fixed value $\overline{\sigma}_{n+1}$.

If the condition $\Phi(\boldsymbol{\Sigma}^{\text{elas}}_{n+1}, f^v_n, \overline{\sigma}_{n+1}) \leq 0$ is met, then the evolution is purely elastic. However, if $\Phi(\boldsymbol{\Sigma}^{\text{elas}}_{n+1}, f^v_n, \overline{\sigma}_{n+1}) > 0$, then the elastic predictor is not plastically admissible and a plastic correction is needed to ensure that the plasticity criterion is verified. In that case, it can be shown that $\Delta\lambda_n$ is the solution of the non-linear equation (Dorhmi et al., 2020)

$$F(\Delta\lambda_n) = \frac{2\overline{\sigma}_{n+1}}{3q_2}\operatorname{argcosh}\left(g(\Delta\lambda_n)\right) + \frac{3\Delta\lambda_n \kappa_n q_1 q_2 f^v_n}{\overline{\sigma}_{n+1}}\sqrt{g(\Delta\lambda_n)^2 - 1} - |\Sigma^{\text{elas}}_{n+1,\text{m}}| = 0, \tag{A.2}$$

where

$$g(\Delta\lambda_n) = \frac{1 + q_3(f^v_n)^2 - \left(\dfrac{\Sigma^{\text{elas}}_{n+1,eq}}{\overline{\sigma}_{n+1} + \dfrac{6\Delta\lambda_n\mu_n}{\overline{\sigma}_{n+1}}}\right)^2}{2q_1 f^v_n} \geq 1. \tag{A.3}$$

In Eqs. (A.2) and (A.3), $\Sigma^{\text{elas}}_{n+1,eq}$ and $\Sigma^{\text{elas}}_{n+1,m}$ are respectively the equivalent and mean parts of the elastic predictor $\boldsymbol{\Sigma}^{\text{elas}}_{n+1}$. Once $\Delta\lambda_n$ is known, all the mechanical fields can be calculated using Eq. (A.1). Then the volume fractions of the three phases are updated using an explicit scheme (at the very end of global elastoplastic iterations, once $\boldsymbol{\epsilon}^{\text{p}}_{n+1}$, $\boldsymbol{\Sigma}_{n+1}$ and $\overline{\epsilon}_{n+1}$ have reached their stationary values):

$$\begin{cases} f^v_{n+1} & = f^v_n + \Delta f^{\text{growth}}_n + \Delta f^{\text{nucleation}}_n \\ f^p_{n+1} & = f^p_n - \theta\Delta f^{\text{nucleation}}_n \\ f^m_{n+1} & = f^m_n - \Delta f^{\text{growth}}_n - (1-\theta)\Delta f^{\text{nucleation}}_n, \end{cases} \tag{A.4}$$

where the increment of volume fraction due to growth $\Delta f^{\text{growth}}_n$ and nucleation $\Delta f^{\text{nucleation}}_n$ are given by

$$\begin{cases} \Delta f^{\text{growth}}_n & = (1 - f^v_n)\text{tr}\Delta\boldsymbol{\epsilon}^{\text{p}}_n \\ \Delta f^{\text{nucleation}}_n & = \dfrac{f_N}{s_N\sqrt{2\pi}}\exp\left[-\dfrac{1}{2}\left(\dfrac{\overline{\epsilon}_{n+1} - \epsilon_N}{s_N}\right)^2\right] \times \Delta\overline{\epsilon}_n. \end{cases} \tag{A.5}$$

In practice, the resolution of the non-linear Eq. (A.2) is done using a Newton method. The algorithm has been implemented numerically into the finite element code Abaqus through a User Material (Umat and Vumat). It must be noted that the tangent operator has not been evaluated since a BFGS method is used for the global iterations.

Appendix B. Sensitivity analysis of nucleation parameters

In this appendix, a sensitivity analysis of the nucleation parameters (ϵ_N, s_N and f_N) is performed. We will study the influence of each parameter taken separately (the others will take the value calibrated). Moreover, in order to appreciate equivalently the sensitivity of the parameters ϵ_N and s_N, we will consider the values $\epsilon_N = [0.02/2;\ 0.02;\ 2 \times 0.02]$ (where $\epsilon_N = 0.02$ is the calibrated value) and $s_N = [0.04/2;\ 0.04;\ 2 \times 0.04]$ (where $s_N = 0.04$ is the calibrated value). For the volume fraction of nucleating voids f_N, we chose the values $f_N = [0.10;\ 0.14;\ 0.18]$ that are close to the volume fraction of particles since these values respectively lead to $\max(f_{\text{nucleation}}) \sim [0.0687;\ 0.0962;\ 0.1237]$.

First, we study the influence of the average nucleation strain ϵ_N by considering the values $\epsilon_N = [0.01;\ 0.02;\ 0.04]$ while keeping $s_N = 0.04$ and $f_N = 0.14$. The evolution of the normalized nucleated volume fraction $f_{\text{nucleation}}/\max(f_{\text{nucleation}})$ and the stiffness loss are represented in Fig. B.1. For the values considered, the influence of the parameter ϵ_N appears to be quite small.

Then, we study the influence of the standard deviation s_N by considering the values $s_N = [0.02;\ 0.04;\ 0.08]$ while keeping $\epsilon_N = 0.02$ and $f_N = 0.14$. The evolution of the normalized nucleated volume fraction $f_{\text{nucleation}}/\max(f_{\text{nucleation}})$ and the stiffness loss are represented in Fig. B.2. The influence of s_N appears to be more pronounced than that of ϵ_N and in that case only the calibrated value appears to be suitable.

We finally study the influence of f_N by considering the values $f_N = [0.10;\ 0.14;\ 0.18]$, while keeping $\epsilon_N = 0.02$ and $s_N = 0.04$. In that case, the evolution of the normalized nucleated volume fraction $f_{\text{nucleation}}/\max(f_{\text{nucleation}})$ is not represented because it only depends on ϵ_N and s_N. The stiffness loss is represented in Fig. B.3. As expected, a decrease of the value f_N leads to a decrease of the stiffness loss (for a given value of θ). It should be noted that a good agreement can also be obtained using either $f_N = 0.10$ (with $\theta = 1$) or $f_N = 0.18$ (with $\theta = 0$). Therefore, the choice of parameters is not unique but this is a standard result using Gurson-type models (see e.g. Springmann and Kuna (2005)). Nonetheless, since the parameter θ corresponds to the overall nucleation ratio, its value can be estimated from the nucleation mechanisms. From the SEM observations of Fig. 4, it can be shown that the damage mechanism is dominated by particle cracking, so that the value of θ should not be either equal to 0 or 1.

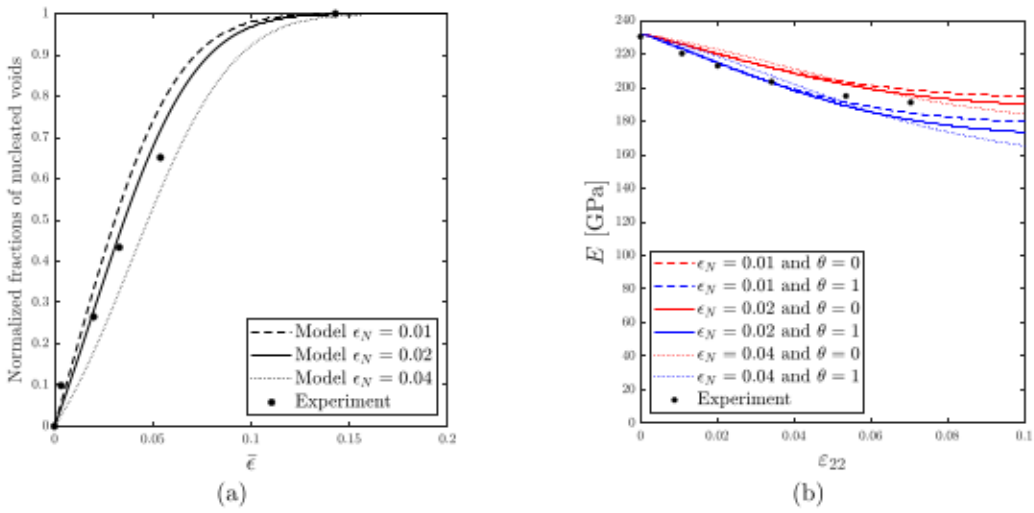

Fig. B.1. Sensitivity analysis of the parameter ϵ_N. (a) Normalized fraction of nucleating voids and (b) Stiffness loss.

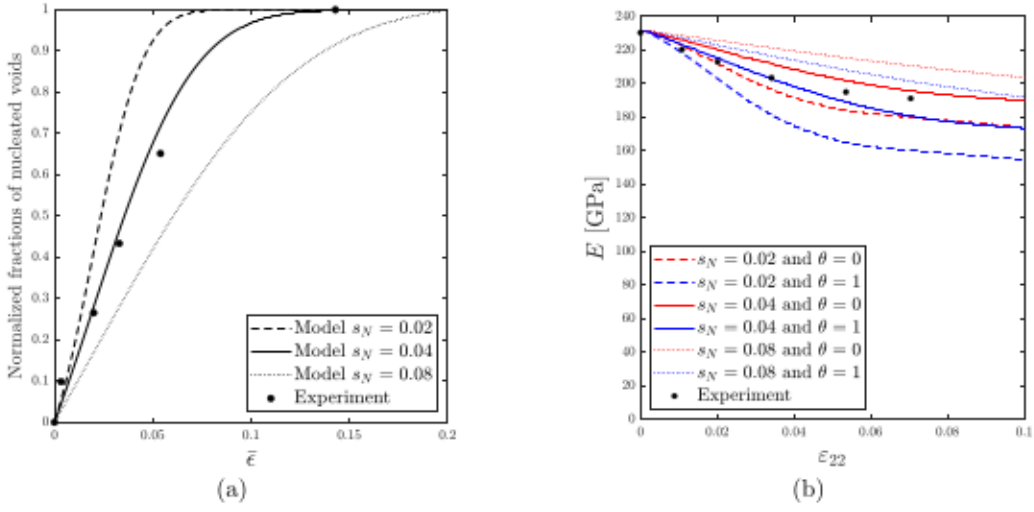

Fig. B.2. Sensitivity analysis of the parameter s_N. (a) Normalized fraction of nucleating voids and (b) Stiffness loss.

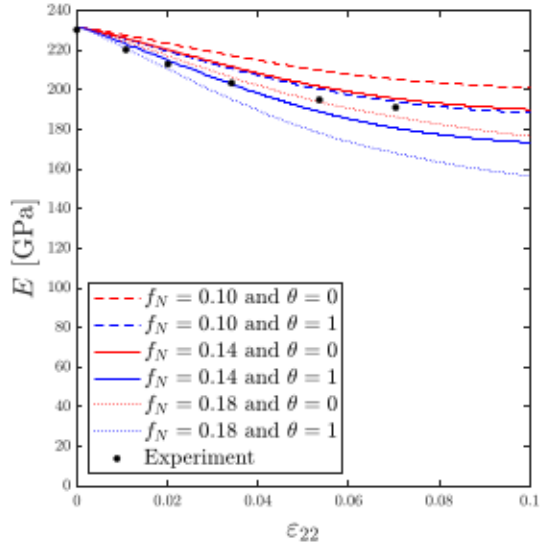

Fig. B.3. Sensitivity analysis of the parameter f_N. Evolution of Young's modulus.

The conclusion of this sensitivity analysis is that the values calibrated, although they are not unique, permit to reproduce quite accurately the experimental results. In addition, small variations (of a few percents) around the values calibrated do not affect much the overall behavior.

References

Amaral, R., Santos, A.D., José, C.d.S., Miranda, S., 2017. Formability prediction for AHSS materials using damage models. J. Phys. Conf. Ser. 843, 012018.

ARCELOR-Research-group, 2008. Patent EP 1 897 963 A1 Bulletin 2008/11, 20.

Bonnet, M., Constantinescu, A., 2005. Inverse problems in elasticity. Inverse Probl. 21.

Bonnet, F., Daeschler, V., Petitgand, G., 2014. High modulus steels: New requirement of automotive market, how to take up challenge? Canad. Metall. Q. 53, 243–252.

Chawla, K.K., 2012. Metal matrix composites. In: Chawla, K.K. (Ed.), Composite Materials: Science and Engineering. Springer New York, New York, NY, pp. 197–248.

Chen, Z., Bong, H.J., Li, D., Wagoner, R.H., 2016a. The elastic–plastic transition of metals. Int. J. Plast. 83, 178–201.

Chen, Z., Gandhi, U., Lee, J., Wagoner, R.H., 2016b. Variation and consistency of Young's modulus in steel. J. Mater Process. Technol. 227, 227–243.

Chu, C.C., Needleman, A., 1980. Void nucleation effects in biaxially stretched sheets. J. Eng. Mater. Technol. 102, 249–256.

Cleveland, R.M., Ghosh, A.K., 2002. Inelastic effects on springback in metals. Int. J. Plast. 18, 769–785.

Derrien, K., Baptiste, D., Guedra-Degeorges, D., Foulquier, J., 1999. Multiscale modeling of the damaged plastic behavior and failure of Al/SiCp composites. Int. J. Plast. 15, 667–685.

Derrien, K., Morin, L., Gilormini, P., 2018. Designing isotropic composites reinforced by aligned transversely isotropic particles of spheroidal shape. Comptes Rendus Mécanique 346, 1123–1135.
Doghri, I., Ouaar, A., 2003. Homogenization of two-phase elasto-plastic composite materials and structures: Study of tangent operators, cyclic plasticity and numerical algorithms. Int. J. Solids Struct. 40, 1681–1712.
Dorhmi, K., Derrien, K., Hadjem-Hamouche, Z., Morin, L., Bonnet, F., Chevalier, J.P., 2021. Experimental study and micromechanical modelling of the effective elastic properties of Fe-TiB2 composites. Compos. Struct. 272, 114122.
Dorhmi, K., Morin, L., Derrien, K., Hadjem-Hamouche, Z., Chevalier, J.P., 2020. A homogenization-based damage model for stiffness loss in ductile metal-matrix composites. J. Mech. Phys. Solids 137, 103812.
Enakoutsa, K., Leblond, J., Perrin, G., 2007. Numerical implementation and assessment of a phenomenological nonlocal model of ductile rupture. Comput. Methods Appl. Mech. Engrg. 196, 1946–1957.
Gaspérini, M., Dammak, M., Franciosi, P., 2017. Stress estimates for particle damage in Fe-TiB2 metal matrix composites from experimental data and simulation. Eur. J. Mech. A Solids 64, 85–98.
González, C., LLorca, J., 2000. A self-consistent approach to the elasto-plastic behaviour of two-phase materials including damage. J. Mech. Phys. Solids 48, 675–692.
Gorji, M.B., Mohr, D., 2018. Predicting shear fracture of aluminum 6016-T4 during deep drawing: Combining Yld-2000 plasticity with Hosford–Coulomb fracture model. Int. J. Mech. Sci. 137, 105–120.
Gurson, A.L., 1977. Continuum theory of ductile rupture by void nucleation and growth: Part I–Yield criteria and flow rules for porous ductile media. ASME J. Eng. Mater. Technol. 99, 2–15.
Hadjem-Hamouche, Z., Chevalier, J.P., Cui, Y., Bonnet, F., 2012. Deformation behavior and damage evaluation in a new titanium diboride (TiB2) steel-based composite. Steel Res. Int. 83, 538–545.
Hadjem-Hamouche, Z., Derrien, K., Héripré, E., Chevalier, J.P., 2018. In-situ experimental and numerical studies of the damage evolution and fracture in a Fe-TiB2 composite. Mater. Sci. Eng. A 724, 594–605.
LLorca, J., Needleman, A., Suresh, S., 1991. An analysis of the effects of matrix void growth on deformation and ductility in metal-ceramic composites. Acta Metall. Mater. 39, 2317–2335.
Morestin, F., Boivin, M., 1996. On the necessity of taking into account the variation in the Young modulus with plastic strain in elastic-plastic software. Nucl. Eng. Des. 162, 107–116.
Mori, T., Tanaka, K., 1973. Average stress in matrix and average elastic energy of materials with misfitting inclusions. Acta Metall. 21, 571–574.
Morin, L., Kondo, D., Leblond, J.B., 2015. Numerical assessment, implementation and application of an extended Gurson model accounting for void size effects. Eur. J. Mech. - A/Solids 51, 183–192.
Mortensen, A., Llorca, J., 2010. Metal matrix composites. Annu. Rev. Mater. Res. 40, 243–270.
Mueller, R., Mortensen, A., 2006. Simplified prediction of the monotonic uniaxial stress–strain curve of non-linear particulate composites. Acta Mater. 54, 2145–2155.
Nicholls, C.J., Boswell, B., Davies, I.J., Islam, M.N., 2017. Review of machining metal matrix composites. Int. J. Adv. Manuf. Technol. 90, 2429–2441.
Okamoto, N.L., Kusakari, M., Tanaka, K., Inui, H., Otani, S., 2010. Anisotropic elastic constants and thermal expansivities in monocrystal CrB2, TiB2, and ZrB2. Acta Mater. 58, 76–84.
Ponte Castaneda, P., Suquet, P., 1997. Nonlinear composites. Adv. Appl. Mech. 34, 171–302.
Saanouni, K., 2008. On the numerical prediction of the ductile fracture in metal forming. Eng. Fract. Mech. 75, 3545–3559.
Segurado, J., LLorca, J., 2002. A numerical approximation to the elastic properties of sphere-reinforced composites. J. Mech. Phys. Solids 50, 2107–2121.
Springmann, M., Kuna, M., 2005. Identification of material parameters of the Gurson–Tvergaard–Needleman model by combined experimental and numerical techniques. Comput. Mater. Sci. 33, 501–509.
Tajdary, P., Morin, L., Romero-Resendiz, L., Gorji, M.B., Braham, C., Gonzalez, G., 2022. Analysis of shear ductile damage in forming processes using a micromechanical model with void shape effects. Int. J. Solids Struct. 248, 111640.
Tekoglu, C., Pardoen, T., 2010. A micromechanics based damage model for composite materials. Int. J. Plast. 26, 549–569.
Tvergaard, V., 1981. Influence of voids on shear band instabilities under plane strain conditions. Int. J. Fract. 17, 389–407.
Tvergaard, V., Needleman, A., 1984. Analysis of the cup-cone fracture in a round tensile bar. Acta Metall. 32, 157–169.
Voyiadjis, G.Z., Kattan, P.I., 1993. Local approach to damage in elasto-plastic metal matrix composites. Int. J. Damage Mech. 2, 92–114.
Wagoner, R.H., Lim, H., Lee, M.G., 2013. Advanced issues in springback. Int. J. Plast. 45, 3–20.
Yeh, H.Y., Cheng, J.H., 2003. NDE of metal damage: Ultrasonics with a damage mechanics model. Int. J. Solids Struct. 40, 7285–7298.
Yoshida, F., Uemori, T., Fujiwara, K., 2002. Elastic–plastic behavior of steel sheets under in-plane cyclic tension–compression at large strain. Int. J. Plast. 18, 633–659.
Zhang, L., Min, J., Carsley, J.E., Stoughton, T.B., Lin, J., 2017. Experimental and theoretical investigation on the role of friction in Nakazima testing. Int. J. Mech. Sci. 133, 217–226.
Zhou, M.Y., Ren, L.B., Fan, L.L., Zhang, Y.W.X., Lu, T.H., Quan, G.F., Gupta, M., 2020. Progress in research on hybrid metal matrix composites. J. Alloys Compd. 838, 155274.